
Attenuation and Scatter Correction in SPECT for Sources in a Nonhomogeneous Object: A Monte Carlo Study

Michael Ljungberg and Sven-Erik Strand

Radiation Physics Department, University of Lund, Lund, Sweden

Single-photon emission computed tomography (SPECT) is important for imaging radioactivity distributions in vivo. Quantitative SPECT is limited due to attenuation and scatter contribution. Approximations such as constant attenuation and mono-exponential scatter functions will not be valid for nonhomogeneous regions. A correction method is described where non-uniform density-maps are used in the attenuation correction. Correction for non-uniform scatter is made by a convolution technique based on scatter line-spread functions (SLSF) calculated for different locations inside a clinically realistic, nonhomogeneous, computer phantom. Calculations have been made for a myocardial source, a uniform source in the lungs and a tumor located in the lungs. Projections were simulated for photon energies corresponding to ^{201}Tl , $^{99\text{m}}\text{Tc}$, and ^{111}In . The results show that quantitative images can be obtained in nonhomogeneous regions. An increased contrast has also been demonstrated in the SLSF-corrected images. Comparison with measurements have been made to validate the Monte Carlo code and the scatter and attenuation method.

J Nucl Med 1991; 32:1278-1284

In diagnostic and oncologic nuclear medicine, SPECT is important for in vivo three-dimensional imaging of activity distributions of radiopharmaceuticals. There are, however, drawbacks with the present SPECT technique in quantitative applications. In most cases, radiopharmaceuticals emitting photons in the energy range 70–250 keV are used. These will be significantly attenuated in the patient. The limited energy resolution of NaI(Tl) (10%–13% FWHM at 140 keV) implies that a large energy window (20%–30%) must be used to maintain accurate counting statistics. This results in ineffective discrimination of photons scattered in the object, which influence the quantification and result in degradation of the image contrast due to misplaced events.

Different attenuation correction methods have been

described in the literature (1–3). A limitation has been the assumption of uniform attenuation which reduces the validity of the correction in nonhomogeneous regions. In such regions, the density distribution must be determined to ensure proper correction. This can be achieved by x-ray-computed tomography or by transmission studies, in which a radioactive flood source is mounted on the scintillation camera (4).

Scatter correction techniques have previously been investigated by other workers (5–12). Among these, convolution-subtraction techniques are based on modeling the scatter in the photo-peak energy window by some scatter function (9–12). The scatter component is estimated by convolving the acquired projection with the scatter function and making a subtraction. The drawback with these methods is that the variation in scatter as a function of source location and density distributions (13) has not adequately been considered.

We present a method that corrects for both nonhomogeneous attenuation and scatter. We have previously shown that the method predicts accurate quantitative results in homogeneous cylindrical phantoms of different sizes (14). In this study, applications of the correction method for clinically realistic source distributions inside a human-like nonhomogeneous phantom are presented.

THE COMPUTATIONAL METHOD

The Monte Carlo simulation is based on uniformly distributed random numbers R to simulate photon histories and selection of different types of interaction processes. The details of the code have been described elsewhere (15) and only a brief description of the parts important for this work is given.

A key feature in this work is the nonhomogeneous computer phantom which simulates a clinically realistic SPECT study. The phantom, denoted $\rho(n, i, j)$, consists of n integer matrices where each matrix describes the density distribution in a particular transverse section of the object. The variation in the mass attenuation coefficients μ/ρ for different materials in the object have been neglected and only one cross-section table is used.

A history is started by sampling a decay position within the source volume. A random number then determines whether the emitted photon escapes the phantom without interaction or if it is scattered inside the phantom.

For the unscattered case, the photon is 'forced' to penetrate

Received Mar. 7, 1990; revision accepted Dec. 17, 1990.
For reprints contact: Michael Ljungberg, PhD, Radiation Physics Department, Lund University Hospital, S-221 85 Lund, Sweden. E-mail: MLJUNGBERG@SELDC52.

the phantom without interaction. The probability for this event is assigned to a history weight W (the probability for the photon to travel the simulated path) and the photon is followed towards the detector.

For the case of a scattered photon, a random number determines the orders of scattering before escaping from the phantom. An isotropic direction is sampled and the distance d_{MAX} to the phantom surface is determined together with the cumulative density per voxel along the path. This is done by following the photon in discrete steps Δd and accumulating the density values closest to the path until the phantom surface has been reached. The probability of interaction within d_{MAX} is calculated from

$$P(\theta, \phi, d_{MAX}) = 1 - \exp[-\Delta d \cdot \mu / \rho \cdot \sum_{\gamma(\theta, \phi)} \rho(n, i, j)], \quad \text{Eq. 1}$$

where γ describes the direction of the photon and thus determines the values of n, i and j . The photon is then 'forced' to interact within d_{MAX} by sampling a truncated photon path, less than or equal to d_{MAX} . Since only one mass-attenuation coefficient table is used, this is equal to sample a truncated 'accumulated density' according to

$$\rho' = \frac{1}{\Delta d \cdot \mu / \rho} \cdot \ln(1 - R \cdot P(\theta, \phi, d_{MAX})), \quad \text{Eq. 2}$$

where R is a random number. The photon is followed from the beginning of the path in the current direction and the density per pixel along the path is again accumulated. The next interaction will be at the point where the accumulated density exceeds ρ' or

$$\sum_{\gamma(\theta, \phi)} \rho(n, i, j) \geq \rho'. \quad \text{Eq. 3}$$

The history weight W is adjusted for the biasing of a truncated path-length. The type of interaction is sampled and the photon is followed as described above, until the sampled number of scattering orders has been simulated. The photon is then 'forced' to be Compton-scattered towards the detector and to escape the phantom without further interaction.

The Nonhomogeneous Phantom

A nonhomogeneous Alderson Rando phantom (Alderson Research Laboratories) of a human skeleton enclosed in a tissue-equivalent Rando plastic (0.985 g cm^{-3} for muscle tissue and 0.32 g cm^{-3} for the lungs) was used. The phantom consisted of multiple transverse sections (thickness 25 mm), where holes (5 mm diameter) have been made in a symmetrical pattern in each of the sections. The distance between the holes was 30 mm. The computer phantom was obtained by an x-ray-computed tomography (Siemens Tomoscanner) of the Rando phantom. Since the relation between the Hounsfield numbers and the density was known, a set of consecutive density maps (256×256 matrix mode, 16-bit integers) was obtained and converted to 64×64 maps by using arithmetic means to obtain a matrix dimension readable by the Monte Carlo code. The pixel size measured $6.8 \times 6.8 \text{ mm}^2$ and the slice thickness was 4.0 mm. The density in the maps was compared with the known density of the lung equivalent material and the tissue equivalent material of the phantom and was found to agree within 5%. A mass attenuation coefficient table for MixD [composition C (77.79%); H (13.40%); Mg (3.86%); O (3.50%); Ti (1.44%)] was used since the exact composition of Rando plastic was not known. An example of a density map is shown in Figure 1.

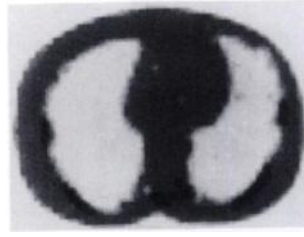


FIGURE 1. A density map of the nonhomogeneous Alderson Rando phantom.

Attenuation Correction

The attenuation correction method, developed by us (4), is based on individual correction factors $K(\theta, r)$ for the original projection data $P_o(\theta, r)$. These factors are calculated from an uncorrected, emission image $E_o(i, j)$ and a density map $\rho(i, j)$. Two projections are calculated from the emission image. The first is simply the line sum of the pixels in $E_o(i, j)$ along the ray-of-view $\gamma(\theta, r)$. The second is obtained by calculating the attenuation from the location corresponding to each pixel to the border along the ray-of-view before making the line summation. Correction factors $K(\theta, r)$ are calculated from the ratio between these two projections

$$K(\theta, r) = \frac{\sum_{\gamma(\theta, r)} E_o(i, j)}{\sum_{\gamma(\theta, r)} [E_o(i, j) \cdot \exp(-\mu d)]}, \quad \text{Eq. 4}$$

where

$$\mu d = \mu / \rho \cdot \Delta s \cdot \sum_{\gamma(\theta, r)} \rho(i, j) \quad \text{Eq. 5}$$

and Δs is the pixel size of $E_o(i, j)$ and $\rho(i, j)$.

Scatter Correction

Two scatter correction techniques have been evaluated in this work. The first is based on a build-up function in the attenuation correction (4,16). The second technique is based on Monte Carlo calculated scatter line spread functions (SLSF) used to model the scatter component in the projections (14).

Build-up functions can be used to quantitatively take into account scatter in a region (a pixel) in the projection. The build-up function is defined by

$$B(\mu d) = \frac{N_p(\mu d) + N_s(\mu, x, y, z)}{N_p(\mu d)}, \quad \text{Eq. 6}$$

where N_p is the events in the region from primary photons and N_s is the events from scattered photons. Both N_p and N_s depend on the object composition and source depth, but N_s also depends on the lateral source distribution. The build-up is included in the attenuation factor according to

$$K(\theta, r) = \frac{\sum_{\gamma(\theta, r)} E_o(i, j)}{\sum_{\gamma(\theta, r)} [E_o(i, j) \cdot B(\mu d) \cdot \exp(-\mu d)]}. \quad \text{Eq. 7}$$

Attenuation and scatter corrected projections, $P_c(\theta, r)$ are obtained from the relation $P_c(\theta, r) = P_o(\theta, r) \cdot K(\theta, r)$.

The SLSF method is based on tabulated SLSFS from point sources at symmetrical positions inside the object. For each angle θ and source locations k , scatter line spread functions $SLSF(\theta, k, r)$ and corresponding scatter-to-total ratios $ST(\theta, k)$ were calculated by the Monte Carlo code. Examples of scatter functions,

calculated for source location 2 in Figure 4A for four projection angles, are shown in Figure 2.

The emission image $E_o(i, j)$ is used to estimate the origin of the scattered photons. The scatter component $P_s(\theta, r)$ in $P_o(\theta, r)$ is estimated by calculating the scatter contribution from the locations in the object corresponding to each of the pixels i, j in E_o . The SLSF(θ, k, r) closest to the apparent location of the pixels are used. The fraction of scattered photons is obtained by multiplying the content in pixel i, j by the $ST(\theta, k)$ and the scatter distribution from location i, j is calculated by convolving the fraction of scattered photons by the selected SLSF(θ, k, r) and add to the scatter component $P_s(\theta, r)$. This is carried out for all pixels in $E_o(i, j)$. Attenuation- and scatter corrected projections, $P_c(\theta, r)$, are obtained from the relation $P_c(\theta, r) = [P_o(\theta, r) - P_s(\theta, r)] \cdot K(\theta, r)$, where $K(\theta, r)$ are evaluated from Equation 4.

System Description

A scintillation camera (Toshiba GCA 901A/ECT) system with a low-energy general-purpose collimator and a medium-energy general-purpose collimator was used for phantom measurements. The NaI(Tl) crystal measured 500×400 mm² and the thickness was 9.52 mm. The energy resolution was 13.2% (FWHM) for 140 keV and the intrinsic spatial resolution was 3 mm (FWHM). The energy window was 30% for 75 keV (²⁰¹Tl) and 20% for both 140 keV (^{99m}Tc) and 247 keV (¹¹¹In). These data were also used for the Monte Carlo simulation.

Phantom Measurements

To verify the Monte Carlo calculations, images of line sources (100 mm length, 0.5 mm diameter) of ²⁰¹Tl, ^{99m}Tc, and ¹¹¹In were obtained at two locations inside the Rando phantom. The position of the sources are indicated in Figure 4A. The activities were 140 MBq for ^{99m}Tc, 2.1 MBq for ²⁰¹Tl, and 5 MBq for ¹¹¹In. The distance between the phantom surface and the collimator was 10 mm. Profiles of thickness 8 mm were defined through the centre of the line source in each image to obtain line spread functions. Monte Carlo simulations were then made for line sources of equal length and identical position inside the phantom.

To evaluate the scatter and attenuation correction methods for a simple but well-known situation, SPECT studies were made using a 22-cm cylindrical water phantom (Data Spectrum Corporation, Chapel Hill, NC). The radius of rotation was 15 cm

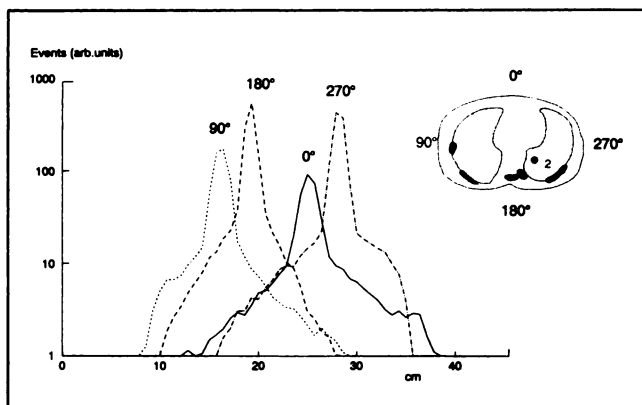


FIGURE 2. Four SLSFs corresponding to four different projections of point source 2, indicated in Figure 4A. The scatter-to-total values (ST) were calculated to 52%, 39%, 33%, and 30% for projection angle 0°, 90°, 180°, and 270°, respectively.

and the acquisitions were made in 60 angles around 360°. Three spherical sources were measured to mimic a hot-lesion case. Uniform distributed activity and spheres containing no radioactive (a cold-lesion case) were also measured. The diameters of the spheres and the off-axis shift is given in Table 1 and the position of the sources is indicated in Figure 3A–B. The acquisition time was 40 sec/frame for the hot-lesion study and 60 sec/frame for the cold-lesion study.

Phantom Simulations

Simulation of clinically realistic sources were made in order to evaluate the quantification in nonhomogeneous regions for 75 keV, 140 keV, and 247 keV photons. The size of the pixels in the density maps was chosen to correspond to a anterior-posterior thickness of about 250 mm. The radius of rotation for the SPECT simulation was 200 mm. Projections (thickness 35 mm) were simulated for 64 angles around 360° and reconstructed to transverse images by filtered backprojection where a Hamming filter was used (cut-off frequency 0.7 cm⁻¹). Corresponding simulations for the sources in “air” were made to serve as references for comparison with corrected images. Photon attenuation and scattering in the source were not allowed in these simulations. The following studies were performed.

Cardiac Simulation. The source consisted of a combined cylinder and a hemisphere, both of radius 40 mm. The source length was 80 mm. Projections were simulated at a location 20 mm from the bottom cylinder surface. Decays were simulated in the volume corresponding to a radius interval of 20 mm–40 mm. The position of the source is indicated in Figure 4C.

Lung Simulation. In this case, a uniform radioactivity distribution within the lungs were simulated. The locations of the source were determined by the information in the computer phantom. Each cell in the phantom with a density within the interval 0.2 g cm⁻³ to 0.6 g cm⁻³ were assigned to be part of the lung volume. Decays were then simulated in the phantom corresponding to the locations of these cells. There is a probability that cells close to the phantom surface will be included as an unwanted part of the source. This was avoided by adding the restriction that the surrounding density cells must be non-zero. The shape and location of the lung sources are shown in Figure 4D.

Tumor Simulation. Three cases of a spherical tumor (radius 25 mm) located in one of the lungs were simulated, namely (1) uniformly distributed source in the tumor only; (2) a cold-lesion situation where the source was distributed in both lungs but not in the tumor; and (3) source concentration ratio of 3:1 between the tumor and the lungs. The source distribution is indicated in Figures 4E and 4F.

Data Evaluation

The studies were corrected for attenuation and scatter using the build-up method and the SLSF method. The calculation of

TABLE 1
The Setup of the Sources for the Cylindrical Water Phantom Measurement

Source no.	Diameter	Off-Axis Shift
1	38.0 mm	55 mm
2	31.8 mm	55 mm
3	25.4 mm	85 mm

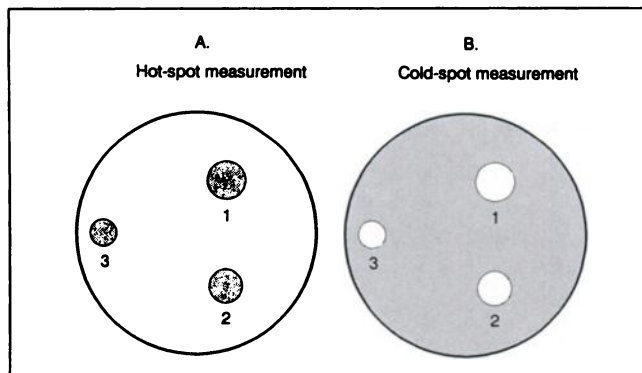


FIGURE 3. The sizes and location of the spheres used in the measurement of the cylindrical water phantom. (A) The hot spot case and (B) the cold spot case.

the build-up functions has been described elsewhere (4). SLSFs were calculated, as described above, for point sources symmetrically located inside the phantom. The distance between the point sources was 40 mm. Sixty-four projections around 360° were also simulated. A mass attenuation coefficient of 0.188 g cm⁻² for 75 keV, 0.154 g cm⁻² for 140 keV, and 0.128 g cm⁻² for 247 keV photons was used for the attenuation correction. The density map in the computer phantom corresponding to the center position of the SPECT projection was used in the attenuation correction. No averaging of opposite projections was performed prior to the attenuation and scatter correction. Before reconstruction, opposite projections were averaged using arithmetic means since the non-linear effects of geometric-means on the attenuation and scatter corrections have not been investigated.

The SPECT studies of the cylindrical water phantom were corrected for scatter, attenuation and physical decay and the measured activity was compared with the known activity. For the cold-lesion case, the measured activity concentrations were compared with the known and the contrast between the three

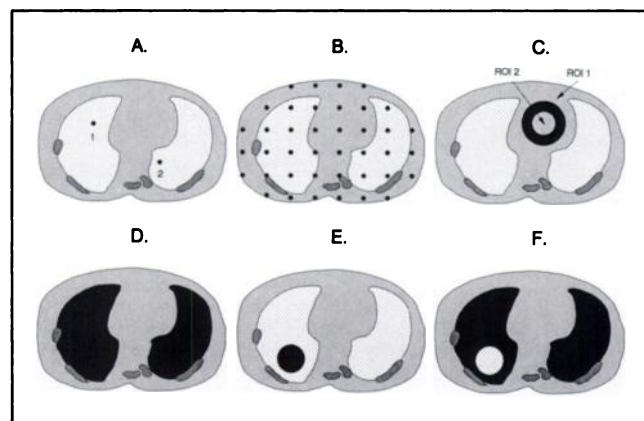


FIGURE 4. The different source location and distributions is shown as black regions. (A) The source locations for the comparison of measured and simulated line-spread functions. (B) The location of point sources for the calculation of the SLSF table SLSF(θ , k , r). (C) The location of the heart source. ROI₁ defines the region where the decays are simulated and ROI₂ defines the inner region. (D) The source distribution for the lung simulation and (E and F) the hot lesion and cold lesion case of the tumor simulation.

cold lesions and the surrounding regions were evaluated from the following contrast definition

$$C = 1 - \left[\frac{N_2/n_2}{N_1/n_1} \right], \quad \text{Eq. 8}$$

where N is the number of events and n is the number of pixels.

For the phantom simulations, a region of interest, ROI₁, was defined which fully covered the source region in the emission images. The events within ROI₁ for uncorrected and corrected images were compared with the “air” images. The contrast between ROI₁ and ROI₂ (indicated in Fig. 4C) where also calculated according to Equation 8. For the lung study, six circular ROIs were defined within the lungs, three in the left lung and three in the right lung, in order to cover most of the lung region. For the tumor study, two circular ROIs were defined where one was covering the tumor and the other in the remaining “healthy” part of the lung.

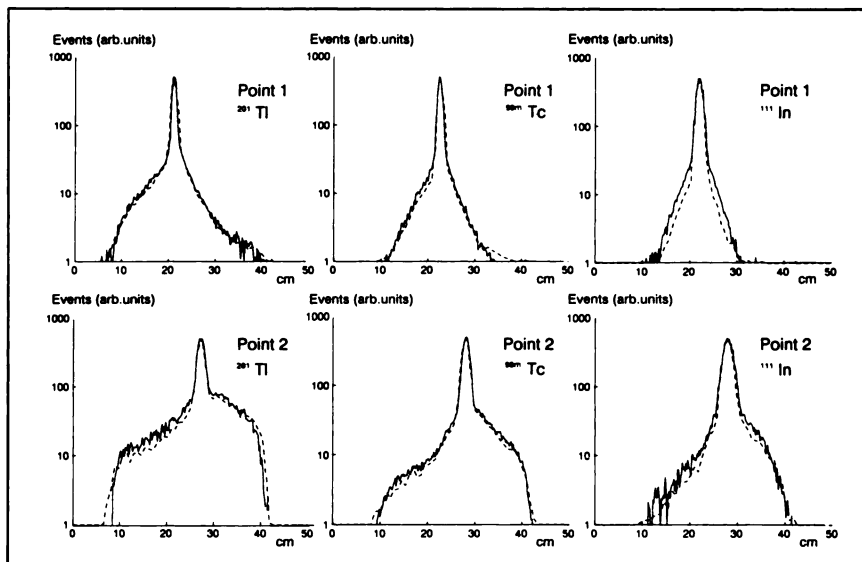
RESULTS

Comparison With Measurements Figure 5 shows a very good agreement between simulated and measured line spread functions. For ²⁰¹Tl, there is a good agreement for the main peak but there is a slight deviation in the scatter tails, especially for location 2. For ^{99m}Tc, there is excellent agreement for both source locations. For ¹¹¹In, the simulated scatter is slightly underestimated for both source locations. The calculations are based on one mass-attenuation coefficient table. The ratio between the mass-attenuation coefficients for bone-equivalent material and MixD are about 0.86, 1.01, and 1.05 for ²⁰¹Tl, ^{99m}Tc, and ¹¹¹In, respectively. Despite the small deviation in the ratios, the results show that the Monte Carlo code predicts accurate SPECT projections of sources inside a nonhomogeneous phantom.

The results from the attenuation and scatter-corrected SPECT studies of the cylindrical water phantom are given in Table 2. The SLSF method gives under-corrected activity values for the hot spot case but gives an estimate of the activity concentration in the cold-spot case with a good accuracy. The build-up method estimates the activity in the spheres better compared with the SLSF method. For the cold spot case, the build-up method overcorrects the activity. It can also be seen from the table that the image contrast has increased in the images corrected by the SLSF method, compared with the build-up corrected images.

Cardiac Simulation There is generally good agreement between corrected data and “air” data, according to Table 3. The build-up method seems, however, to overcorrect the projections for all photon energies, especially for 75 keV photons. The reason for this is not yet understood. For the SLSF method, excellent corrections were achieved for all photon energies, despite a slight over-correction (6%) for 75 keV photons. A contrast enhancement was achieved in the SLSF correction when compared with the build-up method. This is because accurate nonhomogeneous scatter functions are used to model the scatter and that estimated scatter is removed from the projection data

FIGURE 5. A comparison between simulated and measured LSFs obtained from 100-mm line sources of ^{201}Tl , $^{99\text{m}}\text{Tc}$, and ^{111}In at two locations inside the Alderson phantom. The curves have been normalized to the peak values. Measured spread functions are represented by solid lines.



prior to attenuation correction. The contrast was shown to reach the same level as in the “air” images. Table 4 shows also a small decrease in the image contrast for the build-up corrected images. This may be caused by the effect of treating scatter events as primary in the attenuation correction. Further work must, however, be carried out to determine the origin of this contrast reduction.

Lung Simulation Table 3 shows that there is no significant difference between the two correction methods. Both methods predict data very accurately in comparison with the “air” images.

Tumor Simulation Both correction methods undercorrect the single tumor case (Table 3). The events in the ROI relative to the “air” are within 85%–90% for the build-up method and 93% to 96% for the SLSF method. The events in the cold lesion relative to the surrounding region are presented in the lower part of Table 3. It can be observed that the data obtained by the correction methods are in close agreement with the “air” simulation. This is also the case for the hot lesion simulation. The ratio does not approach the true concentration ratio of 3:1 because of

the spill-over of events from the hot lesion to the surrounding region due to the spatial resolution. The reverse is not observed since the source in the surrounding regions is almost uniformly distributed.

DISCUSSION AND CONCLUSION

Quantitative SPECT is highly desirable in both diagnostic and oncologic nuclear medicine. It is, therefore, important to correct for photon attenuation and scatter contribution. In this study, a new attenuation and scatter correction technique based on nonhomogeneous density maps and nonuniform scatter functions have been evaluated for clinically realistic source distributions and radionuclides relevant for many routine clinical studies.

We had earlier developed a convolution subtraction technique for scatter correction that took into account the source depth by using the information in the emission image. The difficult task was to define the scatter functions. In regions with uniform density distribution, the scatter functions may be regarded as independent of the projec-

TABLE 2
Results from the Measurement of Hot and Cold Spheres Inside a Cylindrical Water Phantom

	Source	True activity	No correction	Attenuation correction	
				Build-up	SLSF
Hot lesion	Sphere 1	74 MBq	24 MBq	75 MBq	61 MBq
Total activity	Sphere 2	93 MBq	31 MBq	93 MBq	76 MBq
	Sphere 3	56 MBq	24 MBq	55 MBq	41 MBq
Cold lesion					
Specific activity	Whole phantom	50 kBq/g	22 kBq/g	70 kBq/g	54 kBq/g
Cold lesion					
Contrast	Sphere 1		86%	78%	89%
	Sphere 2		71%	72%	83%
	Sphere 3		69%	75%	72%

* The specific activity has been calculated from several SPECT images of the uniform distributed source.

TABLE 3
Comparison Between Data from Both Uncorrected and Corrected Images^{*}

Study	Energy (keV)	"Air" (%)	Uncorrected (%)	Build-up (%)	SLSF (%)
Cardiac	75	100	23	114	106
	140	100	26	104	99
	247	100	31	102	100
Lungs	75	100	42	105	102
	140	100	43	103	101
	247	100	48	102	102
Single tumor	75	100	27	85	93
	140	100	32	89	95
	247	100	37	90	96
Hot lesion	75	224	188	214	227
	140	223	199	220	231
	247	218	199	215	223
Cold lesion	75	51	68	61	63
	140	36	52	43	44
	247	51	61	55	54

^{*} The results in the upper section are relative to the "air" images (percentage ratio $C_n(\text{phantom})/C_n(\text{air})$ where C is the total count within region n). In the lower part of the table, the results are relative to the surrounding source.

tion angle that reduce the number of required SLSFs. For complex nonhomogeneous objects, a set of scatter functions for each projection angle may be necessary to obtain. The aim of this paper was to show that if those scatter functions are available, quantitative SPECT images can be achieved with a high degree of accuracy.

The results show that clinical realistic projection data can be simulated by the Monte Carlo method using the ray-tracing method described in this paper. In the future with the fast development of computer hardware, Monte Carlo calculation of complex nonhomogeneous objects will probably have a significant impact on research in quantitative SPECT where a knowledge of the limitations of the current systems is important in order to develop better and more accurate correction methods.

It can be seen from Table 2 that the SLSF method underestimates the activity contents after correcting of the hot-spot measurement. This is because the SLSFs used to estimate the scatter is obtained from an integration of the scatter point-spread function. The SLSF functions will thus represent scatter originating from a uniform source distribution around the location of interest. The spherical sources in the hot-spot measurement are, however, lined up at equal axial position. The scatter in a certain pixel will therefore be overestimated by the SLSF method which,

thus, results in an underestimate of the total counts after subtraction.

The build-up function, however, has been developed from a 20-cm line source simulation (4). This corresponds more to the conditions of the measurements. The function should, therefore, be expected to estimate the scatter more accurately, as can be seen in Table 2. The reverse occurs for the cold lesion case, where uniform activity is distributed in the whole phantom. The scatter condition now corresponds more to the basic assumption of the SLSF method as compared with the build-up method. A preliminary result shows a specific activity of 51 kBq/g if a build-up function derived from a thin disc source instead of a line source is used in the correction. The problem can also be seen from the single-tumor simulation. The scatter in the pixels close to the location of the tumor is reduced since no contribution from a peripheral source distribution occur. The scatter as estimated by the two methods will therefore, be too high and result in too low a measurement of the total counts.

These results show that proper scatter correction technique should take into consideration the source distribution in all spatial dimensions (x,y,z). An extension to three-dimensional scatter correction will, however, dramatically increase the computation time and data storage required for the scatter spread functions. An intermediate solution could be to develop build-up functions and SLSFs for a set of different axial source distributions and then choose functions appropriate for the current situation.

Artifacts were found in the lung images corrected by the build-up method (Fig. 6). This is probably because scatter is not removed from the projection data prior to attenuation correction. Problems in the attenuation correction arise close to regions of different density since the method

TABLE 4
The Contrast Calculated Between Region 2 (No Decays) and 1 (Simulated Decays) for the Cardiac Study

Energy (keV)	"Air" (%)	Uncorrected (%)	Build-up (%)	SLSF (%)
75	35	18	13	25
140	33	24	20	33
247	29	22	18	25

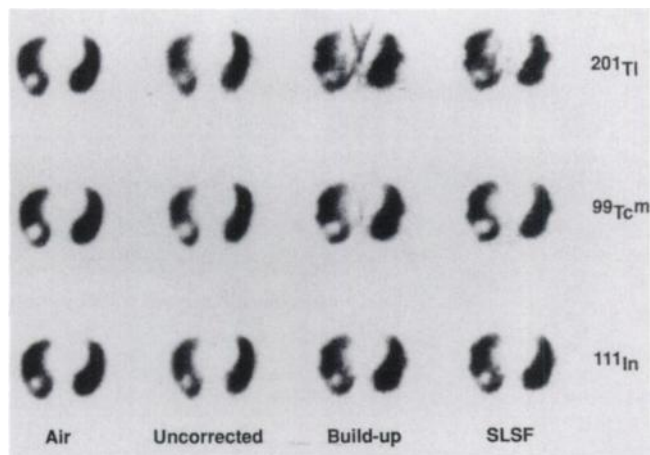


FIGURE 6. Images of a tumor in the lung (cold lesion case) corresponding to "air," no correction, build-up correction and SLSF correction are shown for the different radionuclides.

treat scatter events as primary events when calculating the factor $K(\theta, r)$. This may result in extensive overestimated projection rays observed in the emission images as artifacts. The effect is most pronounced for low photo energies. The figure shows that the SLSF method generates the same type of artifacts, but with a much lower degree because a scatter estimate is subtracted prior to attenuation correction.

In conclusion, quantitative SPECT images can be achieved by using nonhomogeneous attenuation correction based on density maps and by including accurate SLSFs when estimating the scatter component in the projection data. Developing methods that calculate nonhomogeneous scatter functions in general for clinical routine studies is beyond the scope of this paper. We have used the Monte Carlo method which has proven to give reliable results, but the method may be intensely computational. Thus, further work must be carried out to extend the method to a more general level and to optimize the method to make it attractive for routine clinical studies.

ACKNOWLEDGMENTS

The authors thank Marija Ivanovic, PhD, Brookhaven National Laboratory, Upton, NY, John Palmer, PhD and Ingemar

Larsson, Lund University Hospital and Mats Nilsson, PhD, Malmö General Hospital for their assistance with the phantom measurements. This work was supported by grants from the Swedish Cancer Foundation, grant 2353-B87-01XA, 2353-B89-03XA, and 2353-B91-05XAB, the John and Augusta Persson Foundation for Scientific Research, Lund, the Medical Faculty of Lund, and Mrs. Berta Kamprad's Cancer Foundation.

REFERENCES

1. Budinger TF, Gullberg GT, Huesman RH. Emission computed tomography. In: Herman GT, ed. *Image reconstruction from projections: implementation and applications*. New York: Springer Verlag; 1979:147-246.
2. Chang LT. A method for attenuation correction in radionuclide computed tomography. *IEEE Trans Nucl Sci* 1978;25:638-643.
3. Walters TE, Simon W, Chesler DA, et al. Attenuation correction in gamma camera computed tomography. *J Comput Assist Tomogr* 1981;5:89-94.
4. Ljungberg M, Strand S-E. Attenuation correction in SPECT based on transmission studies and Monte Carlo Simulations of build-up functions. *J Nucl Med* 1990;31:493-500.
5. Koral KF, Clinthorne NH, Rogers WL. Improving emission computed tomography quantification by Compton scatter rejection through offset windows. *Nucl Inst Meth in Phys Res* 1986;A242:610-614.
6. Jaszczak RJ, Greer KL, Floyd CE, et al. Improved SPECT quantification using compensation for scattered photons. *J Nucl Med* 1984;25:893-900.
7. Yanch JC, Irvine AT, Webb S, et al. A comparison of deconvolution and windowed subtraction techniques for scatter compensation in SPECT. *IEEE Trans Med Imag* 1988;7:13-20.
8. Mas J, Younes RB, Bidet R. Improvement of quantification in SPECT studies by scatter and attenuation compensation. *Eur J Nucl Med* 1989;15:351-356.
9. Gilardi MC, Bettinardi V, Todd-Pokropek A, et al. Assessment and comparison of three scatter correction techniques in single-photon emission computed tomography. *J Nucl Med* 1988;29:1971-1979.
10. Axelsson B, Msaki P, Israelsson A. Subtraction of Compton-scattered photons in single-photon emission computed tomography. *J Nucl Med* 1984;25:490-494.
11. Msaki P, Axelsson B, Dahl CM, et al. Generalized scatter correction in SPECT using point scatter distribution functions. *J Nucl Med* 1987;28:1861-1869.
12. Mukai T, Links J, Douglass K, et al. Scatter correction in SPECT using non-uniform attenuation data. *Phys Med Biol* 1988;33:1129-1140.
13. Ljungberg M, Strand S-E. Monte Carlo simulated scatter function for non-homogeneous objects [Abstract] *Med Phys* 1989;16:463.
14. Ljungberg M, Strand S-E. Scatter and attenuation correction in SPECT using density maps and Monte Carlo simulated scatter functions. *J Nucl Med* 1990;31:1559-1567.
15. Ljungberg M, Strand S-E. A Monte Carlo program for the simulation of scintillation camera characteristics. *Comput Meth Progr Biomed* 1989;29:257-272.
16. Andersson H, Palmer J, Ljungberg M, et al. Quantitative SPECT by correction of the projection set using transmission data—evaluation of a method. *Eur J Nucl Med* 1990;16:587-594.